Composite Structures 313 (2023) 116913

Contents lists available at ScienceDirect

Composite Structures

journal homepage: www.elsevier.com/locate/compstruct

FRCM-to-masonry bonding behaviour in the case of curved surfaces: Experimental investigation

Tommaso Rotunno [a], Mario Fagone [b,*], Ernesto Grande [c], Gabriele Milani [d]

[a] Department of Architecture, University of Florence, Piazza F. Brunelleschi 6, 50121 Florence, Italy
[b] Department of Civil and Environmental Engineering, University of Florence, Via di S. Marta 3, 50139 Florence, Italy
[c] Department of Engineering Science, University Guglielmo Marconi, Via Plinio 44, 00193 Rome, Italy
[d] Department of Architecture, Built environment and Construction engineering (ABC), Politecnico di Milano, Piazza Leonardo da Vinci 32, 20133, Milan, Italy

ARTICLE INFO

Keywords:
Masonry
Masonry arch
FRCM reinforcements
Curved substrates
Bond characterization

ABSTRACT

Fabric-reinforced cementitious matrix (FRCM) are composite materials more and more used for the reinforcement of masonry structures. The combination of high tensile strength fabrics (or meshes) with cementitious matrices, having good thixotropic capabilities and vapour permeability, makes such composites suitable for reinforcing a large number of masonry structures, including the one belonging to the historic heritage. FRCMs are bonded to the outer surfaces of structural masonry elements and, thanks to their adhesive capacity, bear much of the tensile stresses that unreinforced masonry cannot withstand. The effectiveness of such reinforcements, which is highly dependent on their ability to adhere to the masonry substrate, is generally investigated throughout specific experimental investigations (shear tests). Almost all the papers in the literature devoted to bond-slip analysis refer to the case of flat bonding surfaces, although these reinforcements are also widely used on curved structural elements such as arches and vaults. Therefore, this paper reports and examines the results of an extensive experimental program concerning the behavior of FRCM systems applied on curved masonry specimens. The results point out the influence of both curvature and reinforcement position (intrados or extrados) on the response of specimens in terms of bearing capacity, failure mode and post-peak response.

1. Introduction

In the context of the historic built heritage, masonry structural elements, which are known to be characterized by low tensile strength, very often require adequate reinforcement to bear particular loading conditions.

Several strengthening techniques have been developed and applied to masonry structures over time; the technique increasingly used nowadays consists of the external bonding of specific composite materials (i.e. fabric/mesh and organic/inorganic matrix) on the external surface subjected to tensile stress. In the first decades of the development of this technique, that is since the 1990 s, carbon fiber reinforced polymer (CFRP), composed of an organic matrix and carbon fiber fabric, were almost exclusively used to this purpose [1–4]. Nowadays FRCMs, consisting of inorganic matrices and various types of mesh/fabrics, are preferred due to their better compatibility with the masonry substrate. Indeed, there are many advantages provided by the inorganic matrices over the organic ones: ease of application, greater compatibility with the substrate (even in wet conditions), vapour permeability, reversibility and better behaviour at high temperatures. In such composites, various types of fibers can be used, e.g. carbon, glass, basalt, aramid or polyparaphenylene benzobisoxazole (PBO). These are arranged in fabrics characterized by an open mesh distribution, creating the voids necessary to ensure adhesion between the different mortar layers.

The strength and thixotropic capacity of the inorganic matrices must be such as to ensure the required performance of the reinforcement. The adhesive capacity of the matrix substantially affects the effectiveness of the reinforcement, allowing the tensile stress in the mesh to be transferred to the substrate. Therefore, the mechanical characterization of matrix-to-substrate bonding behaviour assumes a paramount importance; this can be of course determined by carrying out appropriate experimental investigations (e.g. shear tests). Several experimental investigations aimed at this purpose can be found in the literature. Even so, almost all of them analyse the FRCM-to-masonry bond behaviour with reference to flat bonding surfaces [5–15].

The experimental and numerical studies available in literature

* Corresponding author.
E-mail address: mario.fagone@unifi.it (M. Fagone).

https://doi.org/10.1016/j.compstruct.2023.116913
Received 26 September 2022; Received in revised form 23 December 2022; Accepted 8 March 2023
Available online 14 March 2023

[16–20] particularly emphasize the effect of the curved geometry of substrates where the strengthening is applied; normal stresses at the level of mesh-matrix interface, which are generated to satisfy equilibrium conditions, influence the bond performance of FRCM systems. In particular, with respect to applications on flat substrates, in these studies it is pointed out that, while in case of curved specimens strengthened at the extrados, stresses in compression arising at the reinforcement-matrix interface lead to an increase of the bearing capacity and the ductility level, in case of curved specimens strengthened at the intrados, it is generally observed a reduction of the load bearing capacity (premature failures) and a more relevant fragile behavior due to normal stresses in tension. Indeed, differently from flat substrates where the debonding mechanism occurs under the tangential loading only or largely dominated by this failure mode (mode II), in case of curved substrates a coupling between mode II and mode I mechanisms assumes a relevant role in the debonding process. This behaviour, particularly important for the design of strengthening systems for curved masonry structures, and, as underlined in [21,22], for opportunely placing anchor spikes devoted to prevent premature failure phenomena of reinforcements applied at the intrados, is influenced by general parameters, such as the curvature radius and the position of the reinforcement, and by parameters specifically concerning the characteristics of masonry substrate and reinforcement system. The latter, in particular, necessarily require an enrichment of the actual state of the art concerning the experimental characterization of the bond behaviour of FRCM systems applied on curved masonry specimens. This is not marginal, considering the large number of masonry arches and vaults that can potentially be reinforced using this technique [23–28].

Based on the experience gained in a previous extensive experimental and numerical investigation [21,22,29–37] concerning CFRP reinforcements, in this paper the authors present the results of an experimental campaign aimed at studying the FRCM-to-masonry bonding behaviour in the case of both curved and flat surfaces. To this end, straight and curved masonry specimens (identified in the following as "masonry pillars") were considered in the experimental program. Curved pillars, having two different curvatures, are intended as representative of portion of arches; these were reinforced at the intrados or at the extrados with a FRCM composite made of a cementitious-based matrix and a bidirectional PBO mesh. A single lap shear (SLS) test scheme was considered in the experimental program.

The results of the experimental campaign allowed to analyse and characterize the FRCM-to-masonry bond-slip behaviour, also evaluating the effects of the (tensile or compressive) normal stresses that develop at the interface because of the curvature of the bonding surface. In addition, it was possible to analyse the failure modes exhibited by the reinforcements in such situations, which are much more complex with respect to CFRP reinforcements. In fact, as it is well known the detachment of CFRP reinforcements from masonry usually corresponds to a cohesive failure since it is associated to the removal of a thin layer masonry behind the reinforcement; in these cases usually the composite exhibit mainly an elastic behaviour. Much more complex is the failure scenario in the case of FRCM reinforcements. The failure modes experimentally observed in several papers published in the literature (referring to flat bonding surfaces) can be of various types [10]: (i) cohesive debonding in the substrate; (ii) detachment at matrix-to-substrate interface; (iii) detachment at textile-to-matrix interface; (iv) sliding of the textile within the matrix; (v) tensile failure of the textile out of the matrix; (vi) tensile failure of the textile within the matrix.

The paper is organized as follows: next section provide an overall description of the experimental program; the characteristics of the materials used in the experimental program to make the masonry pillars and the reinforcing system are described in section 3; the tensile tests on FRCM coupons and the SLS tests on the reinforced pillars are described in section 4 and section 5 respectively; the experimental outcomes are compared and commented in section 6 and final remarks complete the paper in the last section.

2. Overall description of the experimental program

The experimental campaign presented in this paper was designed to study the behavior of FRCM reinforcements applied to masonry structural elements with curved bonding surface, such as arches and vaults. To this end, masonry pillars with curved axis, representative of portions of arches, reinforced with FRCM were tested considering a SLS test scheme according to [10].

The behavior of the composite reinforcement bonded on curved masonry surfaces was carefully analyzed: pillars with two different curvatures (corresponding to internal radius of 1500 and 3000 mm respectively) and reinforcements bonded at the extrados or at the intrados were considered; furthermore, the experimental outcomes were compared with those obtained with similar straight pillars (i.e. with flat bonding surfaces). The labels referring to the specimen's series and the main geometric characteristics are reported in Table 1. Within each series, the single specimen was identified by the series label followed by a progressive number from 1 to 6.

Tensile tests on the composite material ("Coup" series, comprising six coupons having the same width and thickness of the reinforcement considered for the specimens subjected to SLS tests), tensile tests on the dry mesh ("Mesh" series comprising six specimens having the same width used in the other specimens) carried out according to [38], and experimental tests on the constituent materials (bricks, mortar) complete the experimental investigation.

3. Materials

3.1. Masonry pillars

The masonry pillars (both flat and curved, see Fig. 1) were made using solid pressed bricks (dimensions 250 × 120 × 65 mm) and ready mixed mortar analogous to those used by Authors in previous experimental investigations [21,29,35,39]. The mechanical characterization of these materials has been carried out with specific experimental investigations, published in previous papers to which the reader is referred for more details [4,29,40]. For the sake of completeness, a summary of the main mechanical properties of such materials is reported in the following.

The mean compressive strength and the elastic modulus of the bricks were obtained carrying out compression tests respectively on 18 cubic specimens (50 × 50 × 50 mm^3) and on 6 prismatic specimens (50 × 50 × 150 mm^3); the flexural tensile strength was determined based on three-point bending tests carried out on 6 prismatic specimens (40 × 40 × 200 mm^3), and, finally, the direct tensile strength was determined considering 6 prismatic specimens (40 × 40 × 90 mm^3). A summary of the test results is given in Table 2.

The main mechanical characteristics of the mortar used to realize the masonry pillars were determined according to [41], considering six 40 × 40 × 160 mm^3 subjected to three point bending tests and to compressive tests (carried out on the twelve halves). The mechanical parameters so obtained are summarized in Table 3.

Table 1
Geometric characteristics of the specimen's series considered for SLS tests.

Series	n. spec.	Internal radius [mm]	Bonded length [mm]	Reinf. position
CA-I	6	1500	315	Intrados
CB-I	6	3000	315	Intrados
C0	6	∞	315	–
CB-E	6	3000	339	Extrados
CA-E	6	1500	367	Extrados

Fig. 1. Masonry pillars (both flat and curved).

Table 2
Bricks mechanical properties; CoV = coefficient of variation.

	n. specimens	Mean [MPa]	CoV [%]
Compressive strength	18	20.10	10.79
Young modulus	6	8712	6.92
Direct tensile strength	6	2.49	16.90
Flexural tensile strength	6	3.36	33.77

Table 3
Flexural tensile strength and compressive strength of mortar.

	n. specimens	Mean [MPa]	CoV [%]
Flexural tensile strength	6	1.85	9.42
Compressive strength	12	5.18	8.21

3.2. Constituent materials of the composite reinforcement

The FRCM system considered in this paper was composed of a mortar matrix (M20, according to the technical datasheet) and a bi-directional 70 + 18 g/m^2 PBO mesh (70 g/m^2 in the warp direction and 18 g/m^2 in the weft direction, see Fig. 2).

The indications of UNI EN 1015–11 [41] were considered also to determine the main mechanical characteristics of the mortar matrix of the reinforcing system. The load–displacement diagrams obtained from the bending tests and the compressive stress–strain curves are reported in Fig. 3 (a) and (b) respectively and the main strength values so obtained are summarized in Table 4 together with the coefficient of variation. As can be seen, the test results present a low scattering ad are in line with the strength values declared in the product data sheet, reported in Table 5 together with the declared mechanical properties of the PBO mesh.

The mechanical properties of the PBO mesh in the warp direction were also investigated experimentally through direct tensile tests carried out according to [38]. Six mesh specimens having the geometric characteristics sketched in Fig. 4(a) were reinforced at both ends with CFRP composite tabs to ensure an optimal distribution of the tensile force and to avoid failure mechanisms occurring inside or near the testing machine jaws Fig. 4(b). The tests were carried out at a constant displacement rate of 0.4 mm/min. The specimens were equipped with two linear variable displacement transducers (LVDTs, gauge length 182.5 mm) measuring the elongation of the central part of the mesh

Fig. 2. 70 + 18 g/m^2 bi-directional PBO mesh.

during the tests, which average value was considered to plot the load–displacement diagrams reported in Fig. 4(c). Such equilibrium paths show a quite regular linear branch almost up to the maximum load. Then the tensile failure mechanism, due to the progressive tensile rupture of the fibers, begins in the central part of the specimens and the equilibrium paths show a descending branch until the rupture. Using the equivalent thickness value of the mesh declared by the producer, the tensile strength and elastic modulus values reported in Table 6 were determined. The specimens showed a very regular behavior, as can be seen both from the load–displacement diagrams and from the very low values of coefficient of variation reported in shown in Table 6. Moreover, the experimental elastic modulus of the mesh (average 253 GPa) is close to the value declared by the producer (241 GPa, see Table 5).

4. Tensile tests on FRCM coupons

Six prismatic coupons, comprised of two layers of mortar and a single layer of PBO mesh, were manufactured and tested according to [42] in order to analyse the tensile behaviour of the composite material. The specimens (see Fig. 5) had total thickness of 8 mm (4 mm per mortar layer), length of 500 and width equal to 63 mm; this last value was defined as a multiple of the actual inter-yarn spacing, so that a fabric comprised of 7 yarns could be used to make the coupons.

The specimens were manufactured through a wet-lay-up procedure as suggested by the supplier; in this phase, two wood frames having thickness of 4 mm were used to ensure the correct positioning of the PBO mesh at the midface of the specimen (Fig. 5a).

During curing (curing time minimum 28 days) the specimens were covered with wet clothes and a plastic film in order to minimize the development of differential shrinkage. Moreover, the specimens were stored in standard laboratory conditions for at least seven days before performing the test.

According to [42], during the tests both ends of the specimens were clamped between two stiff steel plates with a rubber sheet in between, as sketched in Fig. 6. In order to prevent both slippage between the steel plates and the coupon and local compressive premature failure in the clamped part of the specimens, a clamping pressure corresponding to 65 % of the (minimum) strength of the mortar (M20, according to the supplier) was imposed.

The specimen was connected at both ends to the testing machine through a double joint as to make spherical hinges, to ensure the alignment between the load and the specimens' axis.

The tests were carried out at a constant rate (0.5 mm/min) of the

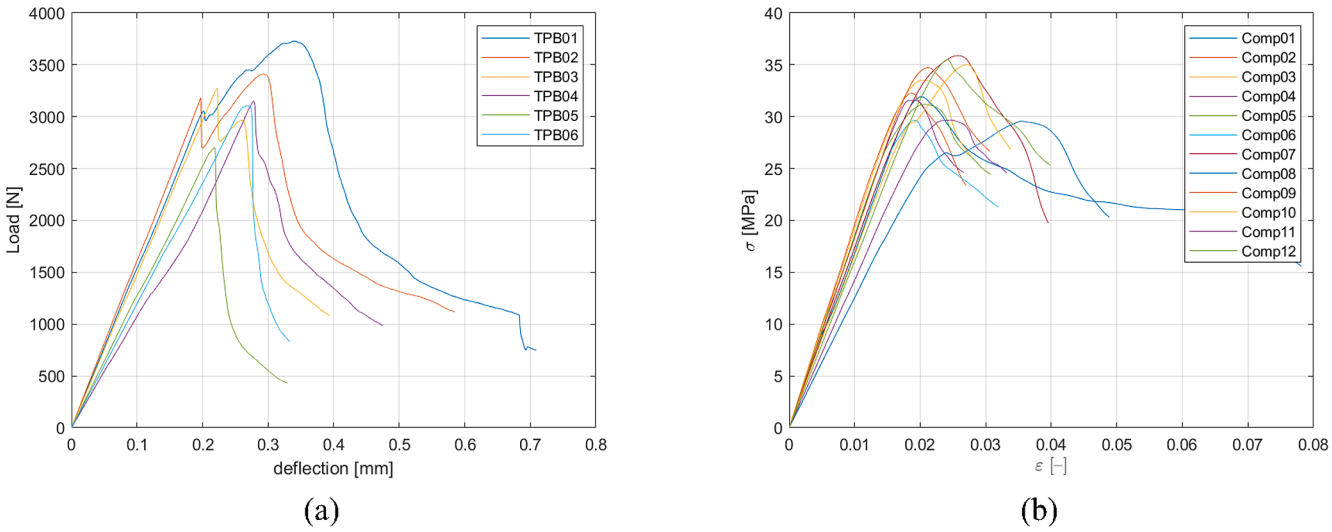

Fig. 3. Mortar matrix of the reinforcing system: (a) three points bending tests load–displacement diagrams and (b) compressive stress–strain diagrams.

Table 4
Flexural tensile strength and compressive strength of the mortar considered in the reinforcing system.

	n. specimens	Mean	CoV
		[MPa]	[%]
Flexural tensile strength	6	7.57	10.61
Compressive strength	12	32.54	7.21

testing machine stroke, corresponding to an average strain rate of the "free" part of the specimen equal to 2×10^{-3}/min.

During the test, two LVDTs measured the elongation of the central portion of the specimen (base length 200 mm, see Fig. 6 (c)). Of course, the total displacement of the testing machine and the load value were also recorded during the tests.

The stress–strain diagrams obtained from the tests are reported in Fig. 7; since the displacement values measured by the two LVDTs during the tests showed no significant rotations during the tests for any of the specimens, the strain values reported in abscissa refer to the average of

Table 5
Mechanical properties (declared by the producer) of the reinforcing system components.

	Equivalent thickness of the warp mesh	Tensile Young's modulus of elasticity E_f of the dry mesh	Ultimate tensile strain of the fibre.	Toughness	Compressive strength at 28 days	Compressive Young's modulus of elasticity at 28 days
	[mm]	[GPa]	[%]	[GPa]	[MPa]	[MPa]
PBO fiber	–	270	2.5	5.80	–	–
Bi-directional PBO mesh	0.045	241	–	–	–	–
Inorganic matrix	–	–	–	–	$\geq$ 20	$\geq$ 7500

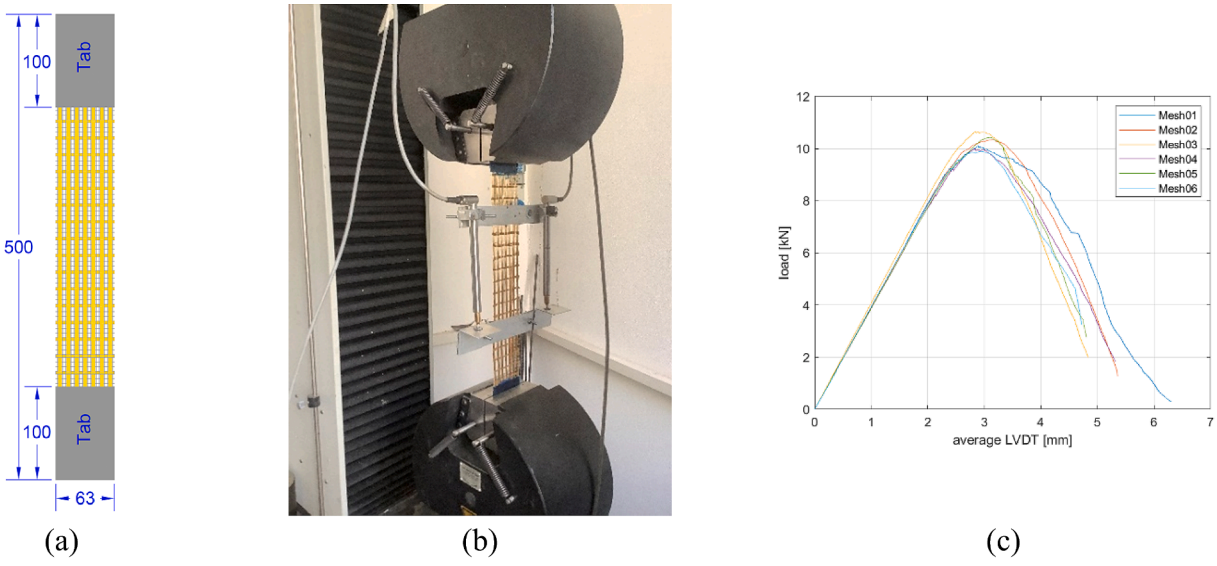

Fig. 4. Tensile tests on dry PBO mesh specimens: (a) geometric characteristics of the specimens (measures in mm); (b) test setup; (c) load–displacement diagrams.

Table 6
Experimental tensile strength and elastic modulus of PBO mesh.

	σ_t [MPa]	E [GPa]
Mesh01	3560	253
Mesh02	3650	252
Mesh03	3758	262
Mesh04	3526	249
Mesh05	3679	249
Mesh06	3490	253
mean	3610	253
CoV [%]	2.83	1.84

the LVDT measurements while the stress values in ordinate refer to the nominal cross section of the mesh $A_f = 63 \times 0.045 mm^2$. The diagrams show the expected typical trilinear shape [11], plus a final descending branch occurring after reaching the maximum load; in fact, the stress–strain diagrams exhibit: at first (stage 1) an almost linear equilibrium path; a second (stage 2) more scattered branch with a lower average slope; a third (stage 3) more regular (with respect to stage 2) and quasi-linear branch up to reaching the maximum load and a final (stage 4) descending unloading branch. As for the development of the crack pattern, stage 1 ended with the formation of the first crack in the mortar, while its progressive development occurred in stage 2. The

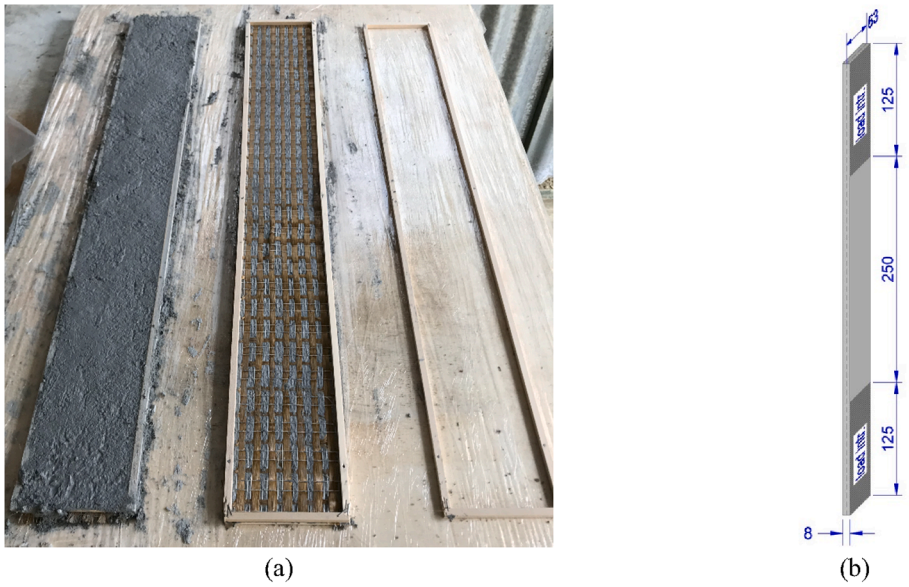

Fig. 5. FRCM coupons: (a) manufacturing process; (b) geometric characteristics (measures in mm).

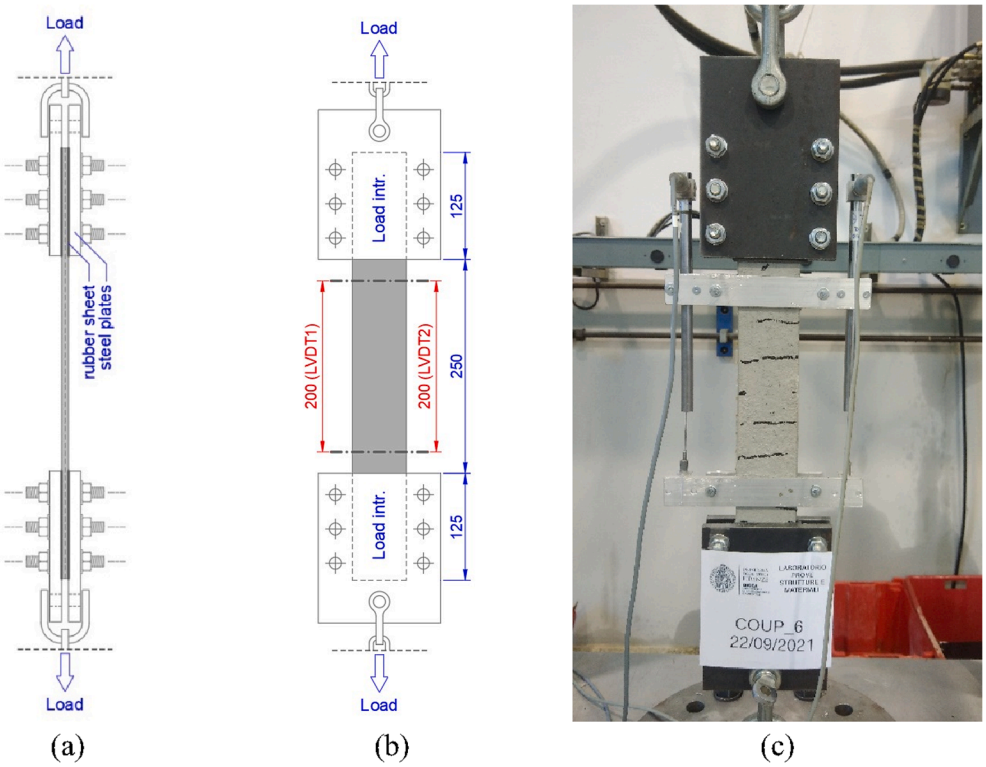

Fig. 6. Tensile tests on FRCM coupons: (a) lateral and (b) front view of the test setup; (c) failure mode.

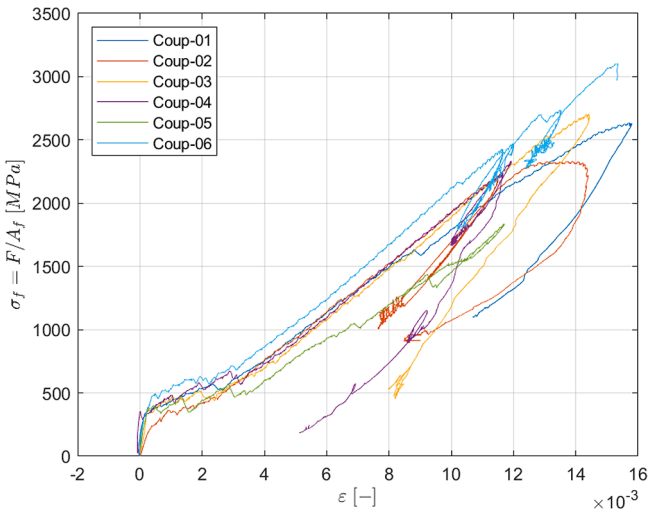

Fig. 7. Stress-Strain diagrams obtained from the tensile tests on coupon specimens.

LVDT's gage length covered a wide portion of the specimen, where most cracks occurred (Fig. 6 (c)), so that the equilibrium path corresponding to this stage exhibits several local peaks and load drops, mainly due to the opening of new cracks. No further cracks occurred in stage 3, where increasing of the global displacement produced the widening of the existing ones. Finally, stage 4 corresponded to the widening of one crack outside the LVDT's gauge length and the shrinking of the other cracks; within this stage, while the global displacement applied to the specimen increased, the load decreased because of the evolution of the failure mechanism of the specimen, due to the tensile failure of the fabric inside the composite ("FTF" = fiber tensile failure, Table 7); for this reason, this stage can be considered as corresponding to the unloading of the portion of the specimen monitored by the LVDTs. In view of the failure mode exhibited by the specimens, according to [42] the stress–strain diagrams are strictly representative of the tensile behaviour of the composite only up to reaching the maximum load (beginning of the crack localization outside the LVDT base length).

The main experimental values obtained from the tests are summarized in Table 7: F_{P_1} refers to the load corresponding to the first crack, F_{max} and $\varepsilon_{F_{max}}$ respectively refer to the maximum load applied to the specimen and to the corresponding average deformation determined via LVDTs, K_1 and K_3 refer to the average slope of the load–displacement (average value of LVDTs) equilibrium paths at stages 1 and 3 respectively. The specimen Coup-04 exhibited some rotations in the initial part of the test (stage 1) so that one of the LVDTs measured negative (i.e. compressive) elongations. For this reason, the first branch of the corresponding load–displacement diagram presents a negative initial stiffness (i.e. $K_1 < 0$, see Fig. 7) which was therefore excluded from the results reported in Table 7. The specimens showed a regular behaviour, given the relatively low values of the coefficient of variation corresponding to the analysed parameters and the analogous failure mode of all the specimens.

Table 7
Main experimental results ("FTF" = fiber tensile failure).

Specimen	F_{P_1} [kN]	F_{max} [kN]	K_1 [kN/mm]	K_3 [kN/mm]	$\varepsilon_{F_{max}}$ [–]	Failure mode
Coup-01	1.033	7.469	17.553	2.572	0.015712	FTF
Coup-02	0.688	6.612	11.158	2.773	0.013890	FTF
Coup-03	1.081	7.670	19.780	2.901	0.014420	FTF
Coup-04	1.011	6.618	–	2.865	0.011919	FTF
Coup-05	1.091	5.206	23.258	2.151	0.011685	FTF
Coup-06	1.403	8.798	19.983	2.931	0.015339	FTF
mean	1.051	7.062	18.346	2.699	0.013828	–
CoV [%]	21.70	17.22	24.55	11.04	12.28	–

Interestingly, the normal stress in the matrix, corresponding to the formation of the first cracks, roughly estimated as the ratio of F_{P_1} to the area of the matrix itself $A_c = 63 \times 8mm^2$ ($F_{P_1}/A_c = 2.1MPa$) corresponds to only 28 % of the flexural tensile strength of the matrix (see Table 4). This difference may be related to the different type of test (direct tensile vs three points bending), different geometry of the specimens (prisms vs layers) and to variations in the effective area of the matrix due to the presence of the horizontal yarns of the mesh (weft direction).

In addition, the ratio of coupon tensile strength F_{max} to the area of the fabric A_f ($f_t = F_{max}/A_f = 2491MPa$) corresponds to 69 % of the experimentally determined mesh tensile strength (see Table 6). This may be due to local effects depending on constraining system used during the tests that may produce stress concentrations and thus local cracking and possible specimen rotations.

5. SLS tests

5.1. Specimens

As described in section 2, the shear tests were carried out on masonry pillars reinforced with PBO-FRCM; both straight and curved specimens were considered for this experimental program, as described in Table 1, which is also referred to for the nomenclature. The masonry pillars are made of five solid pressed bricks (dimensions 250 × 120 × 65 mm) with mortar joints in between having thicknesses as to obtain the considered curvatures; in particular, for the straight pillars the mortar joints have a constant thickness of 10 mm while for the curved specimens the joints have a minimum thickness (at the intrados) of 10 mm and maximum thickness (at the extrados) of 16 and 23 mm for "CB" and "CA" series respectively (see Fig. 8).

The masonry pillars were cured at room conditions for at least 28 days; then, the surface to be reinforced was brushed and cleaned before applying the FRCM reinforcement. According to the technical sheet, a wet-lay-up procedure was used to apply the reinforcement (of course after properly moistening the bonding surface). In particular (see Fig. 9) the first layer of mortar was applied to the specimen making use of a wood frame having thickness of 4 mm; then the mesh was applied, pressing lightly to make it adhere to the mortar; finally, the second layer of mortar way laid making use of another wood frame to ensure the correct positioning of the mesh at the midface of the reinforcement. The bonded area was covered with wet clothes and plastic film and the specimens were kept in plastic bags during the reinforcement curing phase to avoid differential shrinkage and, consequently, cracking or premature debonding of the reinforcement [10].

The reinforcements were made with a single layer of mesh and two layers of mortar matrix, having a thickness of 4 mm each. The width of the reinforcement was 63 mm (as for the coupon specimens; width of mortar after the edge yarn axis equal to 4 mm) and the bonding length ranged between 315 and 367 mm (see Table 1 and Fig. 8) so as to distance of the bonding area from the top and bottom edges of the specimen to avoid stress concentrations. Note that the total length of the mesh was equal to the bond length (portion embedded in the matrix) plus two portions left bare at this stage: the upper one used to apply the load and the lower one (40 mm) used to measure the slip of the free end of the mesh as described in the next section (see Fig. 10).

5.2. Test setup and procedure

Following to [10], the constraining of the specimens was ensured by means of two steel plates positioned at the upper and lower faces and connected by four threaded bars (see Fig. 11), properly pre-tensioned in order to applying a slight precompression to the specimen, avoiding its rotation during the tests. A steel wedge was also used for curved

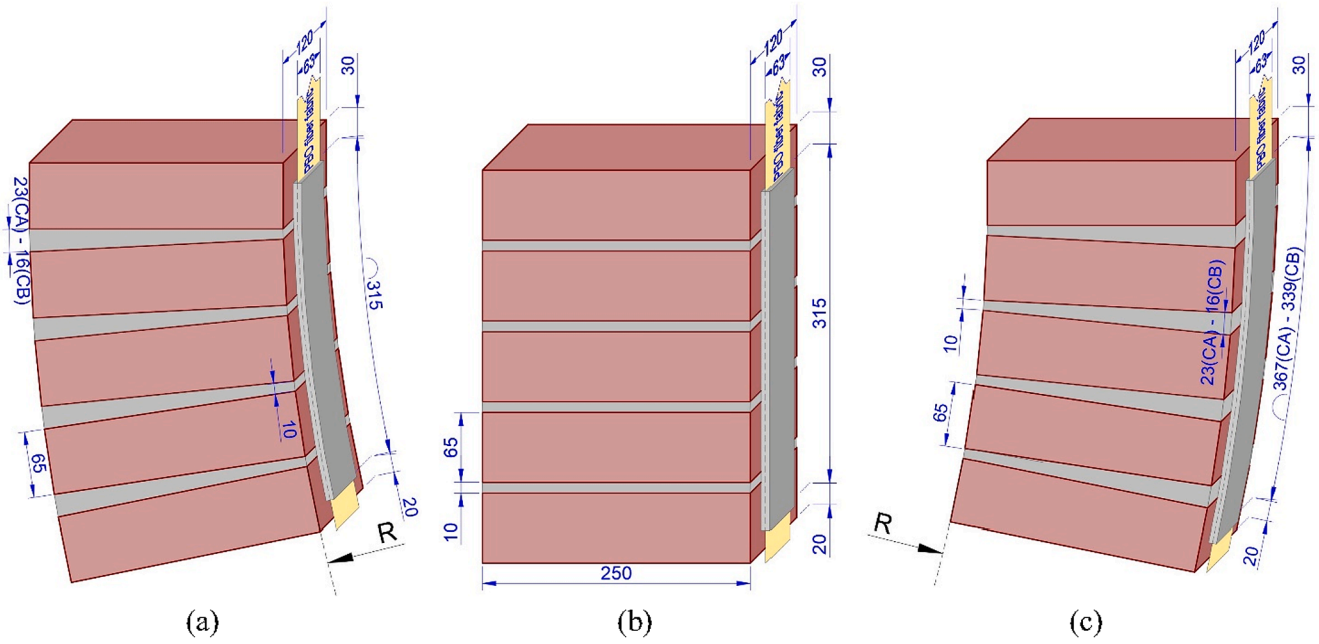

Fig. 8. Geometry of the specimens reinforced at (a) intrados, (b) flat surface and (c) extrados.

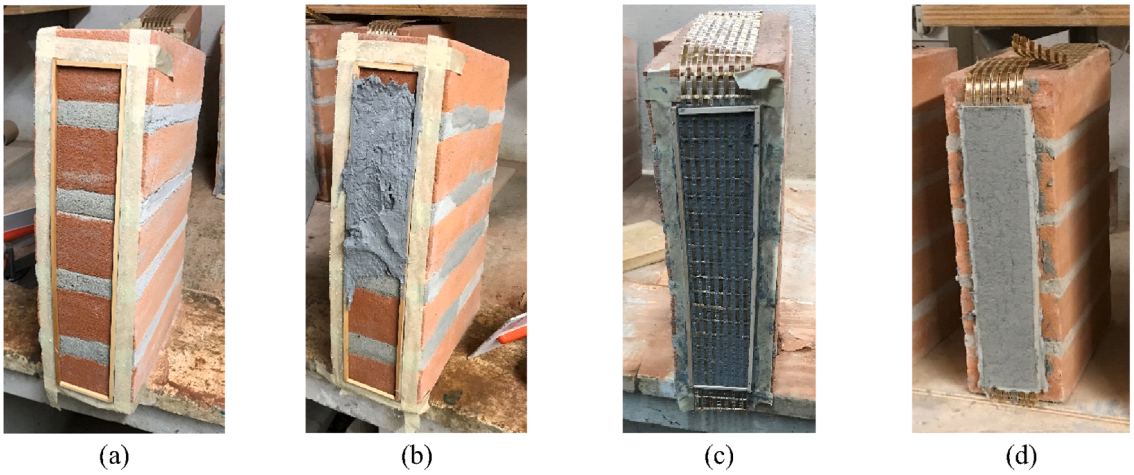

Fig. 9. Preparation of the reinforced masonry pillars: a) first wood frame; b) first layer of mortar; c) application of the PBO mesh and second wood frame; d) second layer of mortar.

specimens to adapt the lower face to the horizontal steel plate connected to the loading machine. The specimens were loaded by clamping the upper side of the bare mesh (i.e. the portion outside the FRCM strengthening), which was previously reinforced with a CFRP composite and equipped with CFRP tabs in order to evenly distribute the load to the reinforcement and to avoid the tensile failure of the mesh outside the composite (see Fig. 12). Note that in applying the CFRP reinforcement to the bare mesh, the FRCM reinforcement was protected to prevent the mortar matrix from touching the epoxy resin.

The specimens were equipped with two couples of LVDTs measuring the slip (relative displacement between the mesh and the masonry substrate) at the upper (loaded) and lower ends of the reinforcements; their position is indicated in red in Fig. 11, Of course, also the load applied to the specimens and the total displacement of the loading machine crosshead were recorded during the tests, which were carried out imposing a machine stroke rate of 0.2 mm/min.

5.3. Results and comments

The load-slip diagrams obtained from the SLS tests, grouped by series, are shown in Fig. 13. The load values correspond to the measurements of the load cell integrated in the testing machine, while the slip value in abscissa refers to the average of the values measured by the LVDTs positioned at the loaded end of the reinforcement (see Fig. 11). All diagrams show a first quasi-linear branch up to the formation of the first cracks and/or an initial detachment at matrix-to-substrate or textile-to-matrix interface [10] at the top (loaded) part of the reinforcement; then, they show a branch with an overall decreasing slope, until the maximum load is reached, within which there is an evolution of the crack pattern and possible detachment phenomena of the reinforcement. Thus, the diagrams show a descending branch and, in many cases, a nearly horizontal final branch corresponding to the sliding of the fabric within the reinforcement. It is noticeable that there is some scatter among the equilibrium paths corresponding to the specimens of the same series. Furthermore, it is evident from the diagrams that, as

Fig. 10. Overall view of half of the specimens, having the free mesh reinforced with CFRP and equipped with CFRP tabs.

expected, the load-bearing capacity is higher for reinforcements applied at the extrados, as are the maximum slip values. Indeed, the curvature of the bonding surface produces normal stresses (at the interface between composite and substrate and between matrix and fabric), namely compressive stresses for reinforcements applied at the extrados and tensile stresses (detrimental, of course) for reinforcements applied at the intrados; the latter, and especially the CA-I series specimens, exhibit according to the test procedure utilized the most brittle behaviour and lower maximum load values.

The main results obtained from the tests and the failure modes of the specimens, determined in accordance with [10], are shown in Table 8. Specifically, K_1 represents the average slope of the first quasi-linear section of the diagrams in Fig. 13, F_b represents the maximum load applied to the specimen, $f_b = F_b/A_f$ and $\tau_{bm} = F_b/A_{bonded}$ represent the peak axial stress in the fabric and the average value of the shear stress in the bonded area respectively, $\eta = f_b/f_t$ (exploitation ratio) represents the ratio between the peak axial stress in the textile f_b and the tensile strength of the coupon referred to the cross-section area of the mesh ($f_t = F_{max\_coupon}/A_f = 2491MPa$, see section 4), s_b denotes the slip corresponding to the maximum load and F_u represents the residual load corresponding to the mesh slip ("D" failure mode). Note that, for reinforcements bonded to curved surfaces, the estimation of τ_{bm} would require a more accurate evaluation of the shear stresses at the bonding surface. Nevertheless, in order to have just an initial comparison among the experimental results, in this paper τ_{bm} is simply estimated as the ratio of F_b to A_{bonded}, deferring more accurate elaborations to further analyses.

Fig. 12. Test setup for SLS tests and positioning of the specimens.

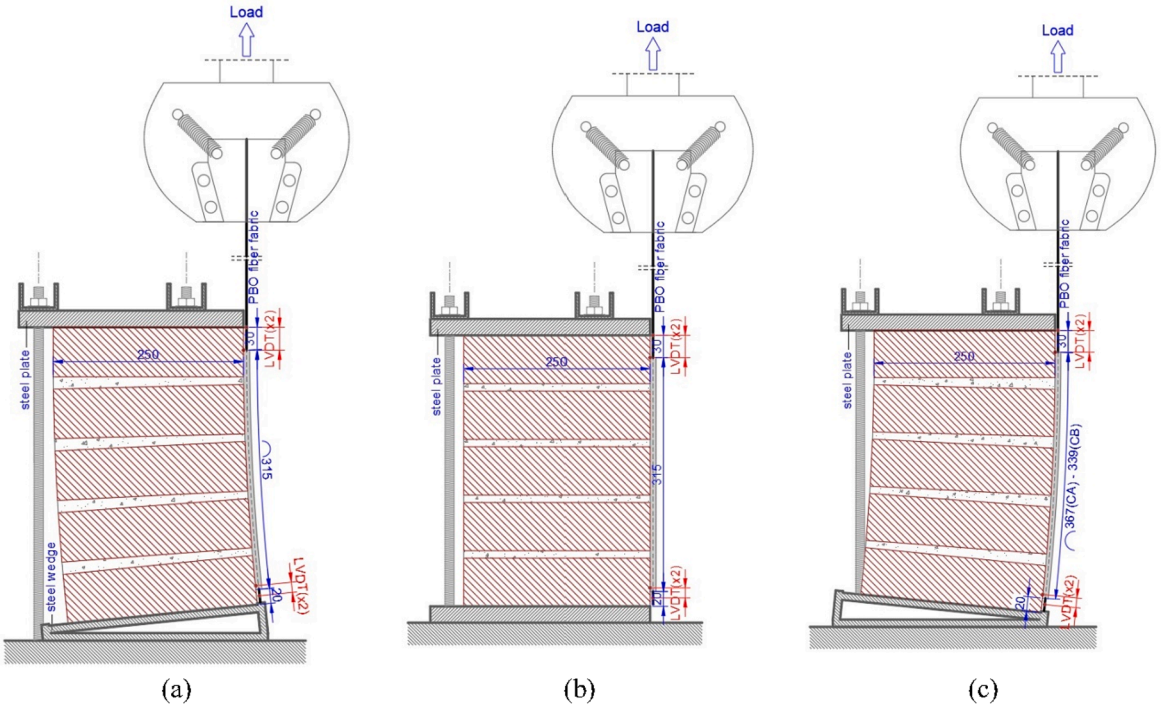

Fig. 11. Schematization of the test setup used for specimens reinforced at (a) intrados, (b) flat surface and (c) extrados.

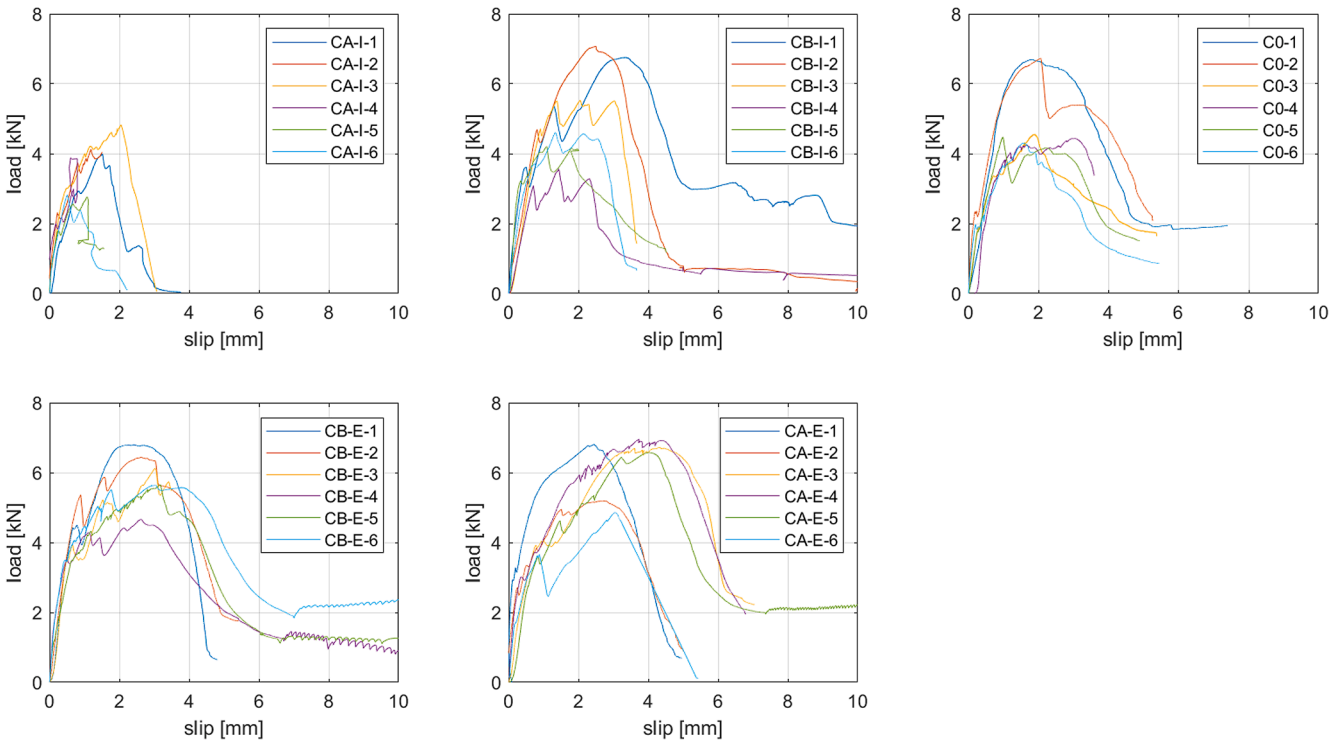

Fig. 13. Load-slip diagrams obtained from the SLS tests.

Table 8
Main experimental results obtained from the SLS tests.K_1 = average slope of the first linear branch of the load-slip diagrams; F_b=maximum load; $f_b = F_b/A_f$ (A_f = nominal cross section area of the mesh); $\tau_{bm} = F_b/(bondedarea)$; $\eta = f_b/f_t$ ($f_t = F_{max}/A_f$ referring to tensile tests on coupons); s_b=slip corresponding to F_b; F_u=residual load corresponding to the mesh slipping ("D" failure mode).

Specimen	K_1	F_b	f_b	τ_{bm}	η	s_b	F_u	F-Mode
	[kN/mm]	[kN]	[MPa]	[MPa]	[–]	[mm]	[kN]	
CA-I-1	7.543	3.995	1409	0.201	0.566	1.505	–	–
CA-I-2	7.806	4.128	1456	0.208	0.585	1.186	–	B
CA-I-3	6.927	4.830	1704	0.243	0.684	2.049	–	B-C
CA-*I*-4	7.838	3.888	1371	0.196	0.551	0.610	–	C
CA-I-5	6.692	2.768	977	0.140	0.392	1.077	–	C
CA-I-6	5.516	2.815	993	0.142	0.399	0.509	–	C
CB-I-1	7.838	6.760	2384	0.341	0.957	3.361	1.828	D-C
CB-I-2	5.862	7.075	2496	0.357	1.002	2.501	0.719	D-E2
CB-I-3	6.290	5.532	1951	0.279	0.783	2.048	–	A-C
CB-*I*-4	5.024	3.576	1261	0.180	0.506	1.432	0.695	C-D
CB-I-5	–	4.208	1484	0.212	0.596	1.092	1.283	C-D
CB-I-6	7.653	4.607	1625	0.232	0.652	1.333	–	C
C0-1	6.469	6.695	2361	0.337	0.948	1.806	1.957	D
C0-2	–	6.731	2374	0.339	0.953	2.066	2.250	D
C0-3	7.089	4.559	1608	0.230	0.646	1.876	1.744	D-C
C0-4	6.121	4.439	1566	0.224	0.629	3.046	–	C-D
C0-5	8.475	4.481	1581	0.226	0.634	0.983	–	C
C0-6	9.773	4.309	1520	0.217	0.610	1.552	0.865	C-D
CB-E-1	9.623	6.809	2402	0.319	0.964	2.399	–	C
CB-E-2	7.820	6.443	2273	0.302	0.912	2.641	1.763	C-D
CB-E-3	10.242	6.124	2160	0.287	0.867	3.016	–	C
CB-E-4	8.587	4.668	1647	0.219	0.661	2.623	1.354	C-D
CB-E-5	9.438	5.657	1995	0.265	0.801	3.177	1.225	C-D
CB-E-6	7.768	5.640	1989	0.264	0.799	3.041	1.981	D
CA-E-1	–	6.810	2402	0.295	0.964	2.452	–	E2
CA-E-2	8.757	5.190	1831	0.224	0.735	2.722	–	E2
CA-E-3	5.547	6.718	2370	0.291	0.951	4.306	2.228	D
CA-E-4	8.597	6.959	2455	0.301	0.985	3.726	1.950	D-C
CA-E-5	6.724	6.576	2320	0.284	0.931	4.016	2.012	D
CA-E-6	10.605	4.856	1713	0.210	0.688	3.049	–	C-D

Again, the symbols suggested by [10] were used to describe the failure modes (see Fig. 14) reported in Table 8. Specifically, "A" denotes "cohesive debonding in the substrate", "B" indicates "detachment at matrix-to-substrate interface", "C" refers to "detachment at textile-to-matrix interface", "D" represents "sliding of the textile within the matrix" and "E2″ denotes the "tensile failure of the textile within the

Fig. 14. Failure modes of the specimens subjected to SLS tests.

matrix“. None of the specimens showed ”tensile failure of the textile out of the matrix“ (denoted by ”E1″ in [10]). “A”, “B”, and “C” failure modes were easily identified during the test; failure modes “D” and “E2” were identified both by comparing the slips measured at the loaded and free end of the mesh and by continuing the application of the displacement after the test was completed, producing the sliding of the mesh within the matrix and verifying its integrity (“D” failure mode) or tensile failure (“E2”).

The specimens reinforced at the intrados predominantly showed “C”-type failure mode, also associated with “B”-type failure mode for the specimens with higher curvature (“CA-I” series) and “D”-type failure mode for the specimens with lower curvature (“CB-I” series); this is related to the detrimental effects of the tensile normal stresses, which may have generated the detachment of a portion of the composite, more evident in the “CA-I” series. For the “C0″ series (flat bonding surface), sliding of the fabric within the matrix (type ”D“ failure) prevails. Finally, for specimens reinforced at the extrados the prevailing failure mode is again ”D,“ associated in some cases with the tensile fibre failure within the composite. In this case, in fact, normal stresses in compression occurring at the interface due to curvature and position of reinforcement lead to a growth of the local bond strength with a consequent increase of the global bearing capacity of the reinforcement, as expected.

6. Comparisons and comments

The mean values and coefficients of variation of the main mechanical parameters deduced from the tests are reported in Table 9 and sketched in Fig. 15 as box charts. In addition, in order to more easily evaluate the effects of curvature on the performance of the reinforcement, the percentage difference between the mean value of the individual parameter compared with the C0 series is also reported Table 9. The values of the coefficients of variation indicate that the statistical dispersion of all examined parameters is acceptable, except for the values of s_b for CA-I series and of both s_b and F_u for CB-I and C0 series. This may be due to the fluctuations shown by the equilibrium paths of the specimens beyond the first linear branch, particularly for CA-I and CB-I series for which the curvature of the reinforcement produces some variability in the failure process. As expected, the load-bearing capacity of the reinforcements tends to increase from specimens reinforced at the intrados to flats and then to specimens reinforced at the extrados. The effect of curvature on the bearing capacity is also in agreement with expectation, since as curvature increases, F_b increases for reinforcements applied at the extrados and decreases for those applied at the intrados. The maximum differences in bearing capacity, compared with the C0 series, are + 19 % for the CA-E series and −28 % for the CA-I series (Table 9). Despite the high values of coefficient of variation mentioned above, the values of s_b show a trend similar to F_b; this is also partly the case for the initial stiffness K_1 of the specimens, which, however, shows a less clear trend. These considerations are also supported by the Δ_{C0} values reported in Table 9, referring to the percentage variation of the specific parameter with respect to C0 series.

Interestingly, CB-I, C0, CB-E and CA-E series show similar values of mean shear stress τ_{bm} (although, as previously described, they have different bonded legth); only CA-I series specimens showed considerably lower values of this parameter with respect to the other series (-28 % compared to the C0 series). According to what previously mentioned, this occurs because of the normal tensile stresses occurring at the interface, due to the increased curvature of the bonding surface. However, note that (as pointed out earlier) τ_{bm} provides just the average value of the tangential stresses at the bonding surface since it is determined simply as the ratio of the maximum load to the bonding area; a more precise estimation of such stress components would require adequate measurement of the strain state in the reinforcement (mesh) [39].

The trend of the exploitation ratio values η (i.e. the ratio of the bearing capacity of the reinforcements to the composite strength esti-

Table 9
Mean values and coefficient of variation (CoV) of the main experimental results obtained from the SLS tests. Δ_{C0} refers to the percentage variation of the specific parameter with respect to C0 series.

		K_1		F_b		F_u		η		s_b	
		[kN/mm]	Δ_{C0} [%]	[kN]	Δ_{C0} [%]	[kN]	Δ_{C0} [%]	[–]	Δ_{C0} [%]	[mm]	Δ_{C0} [%]
CA-I	mean	7.054	−7.01	3.737	−28.16	–	–	0.529	−28.16	1.156	−38.77
	CoV	12.57 %		21.49 %		–		21.49 %		49.59 %	
CB-I	mean	6.533	−13.87	5.293	+1.75	1.131	−29.22	0.750	+1.75	1.961	+3.86
	CoV	18.34 %		26.69 %		47.57		26.69 %		43.79 %	
C0	Mean	7.586	–	5.202	–	1.704	–	0.737	–	1.888	–
	CoV	20.01 %		22.55 %		34.01		22.55 %		36.01 %	
CB-E	mean	8.913	+17.50	5.890	+13.22	1.580	−22.51	0.834	+13.22	2.816	+49.14
	CoV	11.40 %		12.74 %		22.26		12.74 %		10.80 %	
CA-E	Mean	8.046	+6.07	6.185	+18.89	2.063	+1.14	0.876	+18.89	3.379	+78.93
	CoV	24.35 %		14.79 %		7.07		14.79 %		22.09 %	

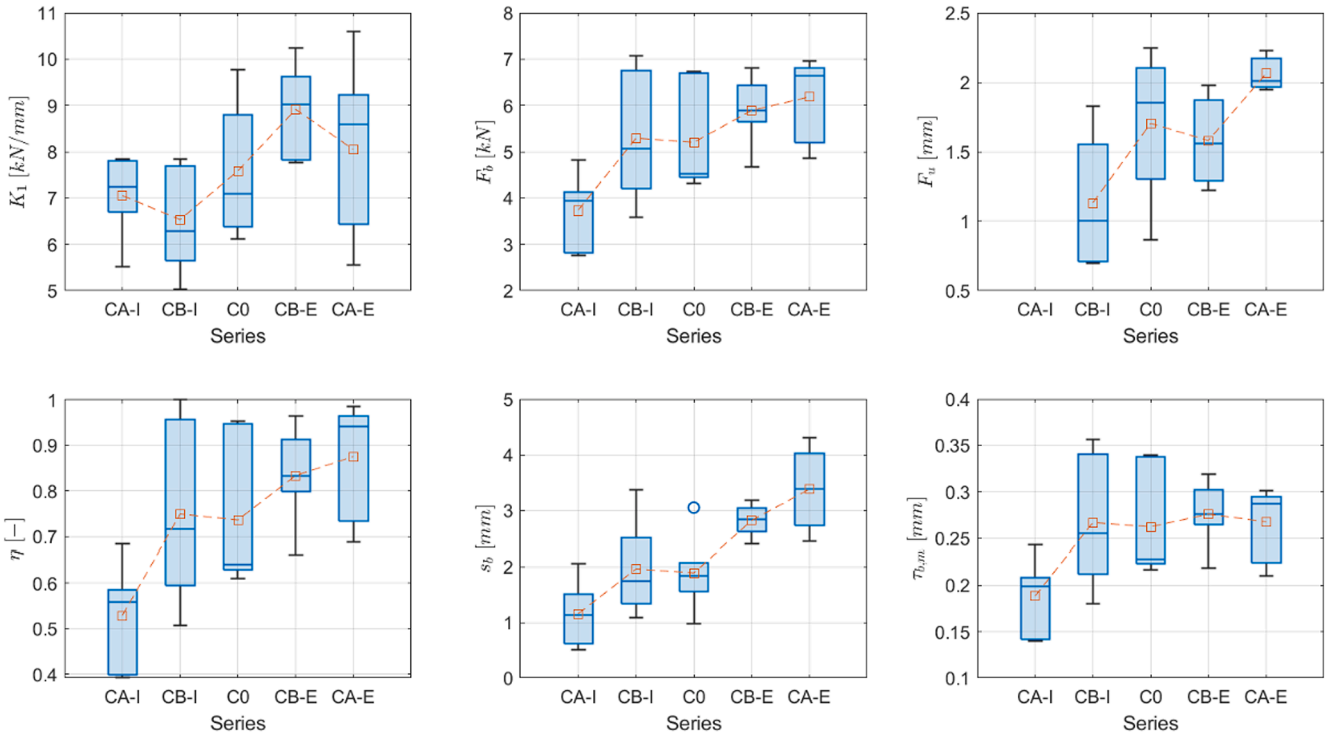

Fig. 15. Box chart diagrams referring to the main experimental results obtained from SLS tests. On each box, the central mark indicates the median, the bottom and top edges of the box indicate the 25th and 75th percentiles, respectively. The whiskers extend to the most extreme data points not considered outliers; the outliers (values that are more than 1.5 times the interquartile range away from the top or bottom of the box) are plotted individually using the 'o' symbol. The mean values within each series are plotted using the "□" symbol.

mated through tensile tests) with respect to reinforcement position and curvature reflects the expectation: it increases for reinforcements applied at the extrados, for which it reaches about 85 %, and decreases for reinforcements applied at the intrados (average value equal to 53 % for the CA-I series); the high values of exploitation ratio highlight that the application of reinforcement at the extrados allows for near-optimal utilization of the bearing capacity of the reinforcement. Even for the flat specimens, significant exploitation ratio values are reached (74 %).

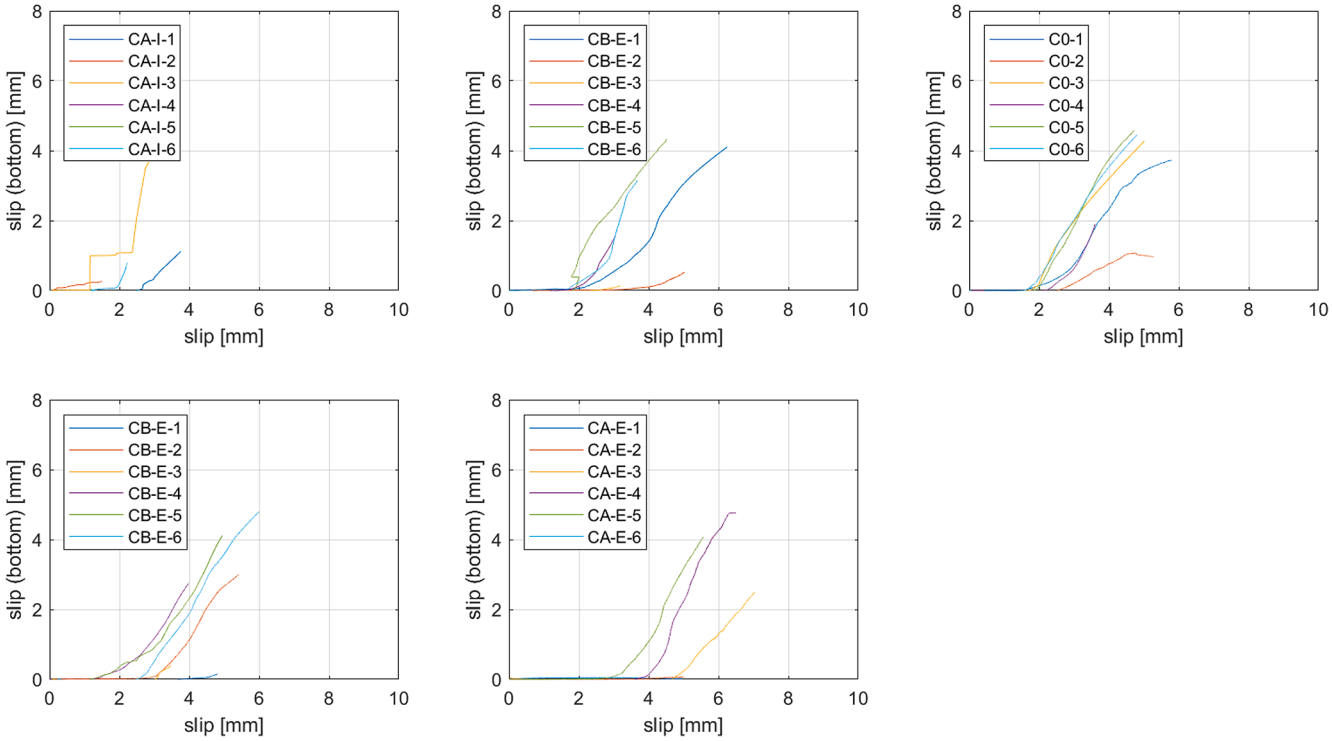

Fig. 16. Slip occurred at the loaded end of the reinforcements vs the analogous parameter occurring at the free end.

The diagrams reported in Fig. 16 allow for comparing the slip measured at the upper (loaded) end of the reinforcement with the analogous slip occurring at the lower end, so that they can be useful also to identify "D" type failure modes. For these specimens, and in cases where the corresponding load-slip diagram shows a nearly horizontal final branch, it is possible to estimate the average friction force F_u occurring at the mesh-to-matrix interface (see Table 8). Obviously, the most significant value is the one corresponding to the C0 series, which is not affected by the effects of curvature. The average values of F_u reported in Table 9 (as well as their coefficients of variation) range between 1.1 kN and 2.1 kN. From the box charts corresponding to F_u, reported in Fig. 15, it can be seen that such residual load increases, with respect to C0, for CB-E and CA-E and decrease for CB-I series.

7. Conclusions

The paper describes the results of an experimental program aimed at characterizing the bond-slip behavior of FRCM reinforcements with PBO mesh bonded to both flat and curved surfaces of masonry structural elements. In the case of reinforcements loaded by in-plane actions and applied to flat surfaces, only tangential stresses are essentially present at the interface. In the case of curved bonding surfaces, on the other hand, in addition to tangential stresses, normal stresses also occur that can substantially change the bond-slip behavior of the reinforcement by improving (in the case of compressive normal stresses) or worsening (in the case of tensile stresses) its behavior. This topic, addressed in the literature in only a few papers, needs to be analyzed in depth as FRCM composites are increasingly used for reinforcing curved masonry structural elements (arches, vaults, etc.); moreover, the complete characterization of the bond-slip behavior of such devices and of the influencing factors is necessary for them to be used in professional practice.

In the experimental program described in this paper, straight and curved specimens of two different types (curvatures), reinforced at the extrados or intrados, were considered. In this way it was possible to evaluate both the (improving) effect of compressive normal stresses and the (worsening) effect of tensile normal stresses occurring at the interface. Experimental results showed that curvature, and thus the sign of normal stresses at the interface, significantly modifies the failure mode of reinforcements as well as their capacity The failure mode of reinforcements applied to flat or extrados surfaces is often associated with fabric creep within the matrix. Experimental results showed that curvature, and thus the sign of normal stresses at the interface, significantly modifies the failure mode of reinforcements as well as their capacity. The failure mode of reinforcements applied to flat or extrados surfaces is often associated with fabric sliding within the matrix. This leads to a final, nearly horizontal branch of the load-slip diagrams from which the residual adhesion between fabric and matrix can be estimated. For proper modeling of such reinforcements, this parameter should be adequately taken into account when defining constitutive laws schematizing the bond-slip behavior. Failure modes associated with fabric sliding are less frequent for reinforcements applied at the intrados and tend not to occur by increasing the curvature of the bonding surface. In such cases, in fact, due to the onset of normal tensile stresses failure is mainly associated to the detachment of the reinforcement from the substrate or of the fabric from the lower layer of mortar matrix. In addition, the curvature and position of the reinforcement (and thus the sign and modulus of the normal stresses at the interface) significantly affect the strength of the reinforcements, and thus modify the bond-slip behaviour. These effects must also be properly considered when defining specific interface models.

In the paper, the variation in bearing capacity, and thus in the exploitation ratio, of the reinforcement is analyzed for all examined conditions. The paper is part of a research activity carried out by the Authors to experimentally and numerically study the bond behavior of FRCM systems externally applied to curved masonry specimens. The outcomes presented in the paper provide an enrichment of the actual state of the art and, moreover, a valuable basis for the development and assessment of numerical models, a subsequent step of the research.

Data availability.

The raw and processed data will be made available on request.

CRediT authorship contribution statement

Tommaso Rotunno: Conceptualization, Investigation, Methodology, Data curation, Writing – original draft, Writing – review & editing. **Mario Fagone:** Conceptualization, Investigation, Methodology, Data curation, Writing – original draft, Writing – review & editing. **Ernesto Grande:** Conceptualization, Investigation, Methodology, Data curation, Writing – original draft, Writing – review & editing. **Gabriele Milani:** Conceptualization, Investigation, Methodology, Data curation, Writing – original draft, Writing – review & editing.

Declaration of Competing Interest

The authors declare that they have no known competing financial interests or personal relationships that could have appeared to influence the work reported in this paper.

Data availability

Data will be made available on request.

References

[1] Triantafillou TC. Strengthening of masonry structures using epoxy-bonded FRP laminates. J Compos Constr 1998;2:96–104.
[2] Valluzzi MR, Oliveira DV, Caratelli A, Castori G, Corradi M, de Felice G, et al. Round Robin Test for composite-to-brick shear bond characterization. Mater Struct 2012;45:1761–91. https://doi.org/10.1617/s11527-012-9883-5.
[3] Rotunno T, Rovero L, Tonietti U, Briccoli BS. Experimental Study of Bond Behavior of CFRP-to-Brick Joints. J Compos Constr 2015;19:04014063. https://doi.org/10.1061/(ASCE)CC.1943-5614.0000528.
[4] Fagone M, Ranocchiai G, Caggegi C, Briccoli Bati S, Cuomo M. The efficiency of mechanical anchors in CFRP strengthening of masonry: an experimental analysis. Compos Part B Eng 2014;64:1–15. https://doi.org/10.1016/j.compositesb.2014.03.018.
[5] De Santis S, Carozzi FG, de Felice G, Poggi C. Test methods for Textile Reinforced Mortar systems. Compos Part B Eng 2017;127:121–32. https://doi.org/10.1016/j.compositesb.2017.03.016.
[6] Lignola GP, Caggegi C, Ceroni F, De Santis S, Krajewski P, Lourenço PB, et al. Performance assessment of basalt FRCM for retrofit applications on masonry. Compos Part B Eng 2017;128:1–18. https://doi.org/10.1016/j.compositesb.2017.05.003.
[7] D'Antino T, Calabrese AS, Poggi C. Experimental procedures for the mechanical characterization of composite reinforced mortar (CRM) systems for retrofitting of masonry structures. Mater Struct Constr 2020;53:1–18. https://doi.org/10.1617/S11527-020-01529-1/FIGURES/11.
[8] Leone M, Aiello MA, Balsamo A, Carozzi FG, Ceroni F, Corradi M, et al. Glass fabric reinforced cementitious matrix: tensile properties and bond performance on masonry substrate. Compos Part B Eng 2017;127:196–214. https://doi.org/10.1016/j.compositesb.2017.06.028.
[9] Carozzi FG, Bellini A, D'Antino T, de Felice G, Focacci F, Hojdys Ł, et al. Experimental investigation of tensile and bond properties of Carbon-FRCM composites for strengthening masonry elements. Compos Part B Eng 2017;128:100–19. https://doi.org/10.1016/j.compositesb.2017.06.018.
[10] de Felice G, Aiello MA, Caggegi C, Ceroni F, De Santis S, Garbin E, et al. Recommendation of RILEM Technical Committee 250-CSM: Test method for Textile Reinforced Mortar to substrate bond characterization. Mater Struct Constr 2018:51. https://doi.org/10.1617/s11527-018-1216-x.
[11] Caggegi C, Carozzi FG, De Santis S, Fabbrocino F, Focacci F, Hojdys Ł, et al. Experimental analysis on tensile and bond properties of PBO and aramid fabric reinforced cementitious matrix for strengthening masonry structures. Compos Part B Eng 2017;127:175–95. https://doi.org/10.1016/j.compositesb.2017.05.048.
[12] De Santis S, Ceroni F, de Felice G, Fagone M, Ghiassi B, Kwiecień A, et al. Round Robin Test on tensile and bond behaviour of Steel Reinforced Grout systems. Compos Part B Eng 2017;127:100–20. https://doi.org/10.1016/j.compositesb.2017.03.052.
[13] Bellini A, Aiello MA, Bencardino F, de Carvalho Bello CB, Castori G, Cecchi A, et al. Influence of different set-up parameters on the bond behavior of FRCM composites. Constr Build Mater 2021;308:124964. https://doi.org/10.1016/j.conbuildmat.2021.124964.

[14] D'Ambrisi A, Feo L, Focacci F. Experimental and analytical investigation on bond between Carbon-FRCM materials and masonry. Compos Part B-Engineering 2013; 46:15–20. https://doi.org/10.1016/J.Compositesb.2012.10.018.
[15] Olivito RS, Codispoti R, Cevallos OA. Bond behavior of Flax-FRCM and PBO-FRCM composites applied on clay bricks: experimental and theoretical study. Compos Struct 2016;146:221–31. https://doi.org/10.1016/J.COMPSTRUCT.2016.03.004.
[16] Malena M, de Felice G. Debonding of composites on a curved masonry substrate: experimental results and analytical formulation. Compos Struct 2014;112: 194–206. https://doi.org/10.1016/j.compstruct.2014.02.004.
[17] De Santis S. Bond behaviour of Steel Reinforced Grout for the extrados strengthening of masonry vaults. Constr Build Mater 2017;150:367–82. https://doi.org/10.1016/J.CONBUILDMAT.2017.06.010.
[18] Malena M. Closed-form solution to the debonding of mortar based composites on curved substrates. Compos Part B Eng 2018;139:249–58. https://doi.org/10.1016/J.COMPOSITESB.2017.11.044.
[19] Misseri G, Stipo G, Rovero L. Bond Behaviour of PBO FRCM on Curved Masonry Substrates. Lect Notes. Civ Eng 2022:198. https://doi.org/10.1007/978-3-030-88166-5_178/FIGURES/6. LNCE:2060-72.
[20] Grande E, Milani G. Modeling of FRCM strengthening systems externally applied on curved masonry substrates. Eng Struct 2021;233:111895. https://doi.org/10.1016/J.ENGSTRUCT.2021.111895.
[21] Rotunno T, Fagone M, Bertolesi E, Grande E, Milani G. Curved masonry pillars reinforced with anchored CFRP sheets: an experimental analysis. Compos Part B Eng 2019:174. https://doi.org/10.1016/j.compositesb.2019.107008.
[22] Bertolesi E, Milani G, Fagone M, Rotunno T, Grande E. Heterogeneous FE model for single lap shear tests on FRP reinforced masonry curved pillars with spike anchors. Constr Build Mater 2020;258:119629. https://doi.org/10.1016/j.conbuildmat.2020.119629.
[23] Garmendia L, Marcos I, Garbin E, Valluzzi MR. Strengthening of masonry arches with Textile-Reinforced Mortar: experimental behaviour and analytical approaches. Mater Struct Constr 2014:47. https://doi.org/10.1617/s11527-014-0339-y.
[24] Valvona F, Toti J, Gattulli V, Potenza F. Effective seismic strengthening and monitoring of a masonry vault by using Glass Fiber Reinforced Cementitious Matrix with embedded Fiber Bragg Grating sensors. Compos Part B Eng 2017;113: 355–70. https://doi.org/10.1016/J.COMPOSITESB.2017.01.024.
[25] Alecci V, Focacci F, Rovero L, Stipo G, De Stefano M. Intrados strengthening of brick masonry arches with different FRCM composites: experimental and analytical investigations. Compos Struct 2017;176:898–909. https://doi.org/10.1016/J.COMPSTRUCT.2017.06.023.
[26] Carozzi FG, Poggi C, Bertolesi E, Milani G. Ancient masonry arches and vaults strengthened with TRM, SRG and FRP composites: experimental evaluation. Compos Struct 2018;187:466–80. https://doi.org/10.1016/j.compstruct.2017.12.075.
[27] De Santis S, Roscini F, de Felice G. Strengthening of masonry vaults with textile reinforced mortars, springer. Cham 2019:1539–47. https://doi.org/10.1007/978-3-319-99441-3_165.
[28] Ramaglia G, Gian ;, Lignola P, Balsamo A, Prota A, Manfredi G. Seismic Strengthening of Masonry Vaults with Abutments Using Textile-Reinforced Mortar. J Compos Constr 2016;21:04016079. Doi: 10.1061/(ASCE)CC.1943-5614.0000733.
[29] Rotunno T, Fagone M, Bertolesi E, Grande E, Milani G. Single lap shear tests of masonry curved pillars externally strengthened by CFRP strips. Compos Struct 2018;200:434–48. https://doi.org/10.1016/j.compstruct.2018.05.097.
[30] Grande E, Fagone M, Rotunno T, Bertolesi E, Milani G. Coupled interface-based modelling approach for the numerical analysis of curved masonry specimens strengthened by CFRP. Compos Struct 2018;200:498–506. https://doi.org/10.1016/j.compstruct.2018.05.118.
[31] Bertolesi E, Grande E, Fagone M, Milani G, Rotunno T. Mechanical model based on a BVP for FRPs applied on flat and curved masonry pillars with anchor spikes. Compos Struct 2021:273. https://doi.org/10.1016/j.compstruct.2021.114251.
[32] Bertolesi E, Milani G, Fagone M, Rotunno T, Grande E. Micro-mechanical FE numerical model for masonry curved pillars reinforced with FRP strips subjected to single lap shear tests. Compos Struct 2018;201:916–31. https://doi.org/10.1016/j.compstruct.2018.06.111.
[33] Grande E, Fagone M, Rotunno T, Bertolesi E, Milani G. Modelling of the bond behaviour of curved masonry specimens strengthened by CFRP with anchor spikes. Compos Part B Eng 2019;171:235–45. https://doi.org/10.1016/j.compositesb.2019.04.027.
[34] Grande E, Milani G, Bertolesi E, Fagone M, Rotunno T. Modeling of the Tensile Behavior FRCM Systems for Repair and Strengthening Interventions of Masonry Structures. Front Built Environ 2020;6:51. https://doi.org/10.3389/fbuil.2020.00051.
[35] Fagone M, Rotunno T, Bertolesi E, Grande E, Milani G. An experimental study on the effectiveness of cfrp reinforcements applied to curved masonry pillars. In: Carcaterra A, Paolone A, Graziani G, editors. Lect. Notes Mech. Eng., Rome: Springer, Cham; 2020, p. 2134–48. Doi: 10.1007/978-3-030-41057-5_170.
[36] Milani G, Fagone M, Rotunno T, Grande E, Bertolesi E. Development of an interface numerical model for C-FRPs applied on flat and curved masonry pillars. Compos Struct 2020;241:112074. https://doi.org/10.1016/j.compstruct.2020.112074.
[37] Milani G, Grande E, Bertolesi E, Rotunno T, Fagone M. Debonding mechanism of FRP strengthened flat surfaces: analytical approach and closed form solution. Constr Build Mater 2021;302:124144. https://doi.org/10.1016/J.CONBUILDMAT.2021.124144.
[38] Consiglio Superiore dei Lavori Pubblici - Serevizio Tecnico Centrale. Linea Guida per la identificazione, la qualificazione ed il controllo di accettazione di compositi fibrorinforzati a matrice inorganica (FRCM) da utilizzarsi per il consolidamento strutturale di costruzioni esistenti 2018.
[39] Bertolesi E, Fagone M, Rotunno T, Grande E, Milani G. Experimental characterization of the textile-to-mortar bond through distributed optical sensors. Constr Build Mater 2022;326:126640. https://doi.org/10.1016/J.CONBUILDMAT.2022.126640.
[40] Fagone M, Ranocchiai G, Briccoli BS. An experimental analysis about the effects of mortar joints on the efficiency of anchored CFRP-to-masonry reinforcements. Compos Part B-Eng 2015;76:133–48. https://doi.org/10.1016/j.compositesb.2015.01.050.
[41] UNI EN 1015-11. Methods of test for mortar for masonry Part 11: Determination of flexural and compressive strength of hardened mortar 2007;UNI EN 101.
[42] Brameshuber W, Hinzen M, Dubey A, Peled A, Mobasher B, Bentur A, et al. Recommendation of RILEM TC 232-TDT: test methods and design of textile reinforced concrete: Uniaxial tensile test: test method to determine the load bearing behavior of tensile specimens made of textile reinforced concrete. Mater Struct Constr 2016;49:4923–7. https://doi.org/10.1617/s11527-016-0839-z.